Time domain cyclostationarity signal processing tools

François Léonard

Institut de recherche d'Hydro-Québec – IREQ
1800 Lionel-Boulet, Varennes (QC), Canada J3X 1S1
leonard.françois@ireq.ca

Abstract

This paper proposes four different time-domain tools to estimate first-order cyclostationarity signals. These methods appear intuitively simpler than first-order and higher-order spectra, offer user-friendly graphic interfaces to visualize a pattern, allow the retrieval and removal of the selected cyclostationarity components and, when using an adaptive resampled signal, can deal with time-varying operating conditions where a phase blur reduces the estimation efficiency of the spectra. Three coherency indicators are proposed, one for every sample of the time pattern, one for each impact (tooth shock) observed in the pattern, and one for the whole pattern. These indicators are used to detect a cyclostationarity and analyze the pattern repeatability. A gear mesh graph is also proposed to illustrate the cyclostationarity in 3D.

1 Introduction

The work presented here was carried out without considering the state of the art of cyclostationarity. In fact, a literature search revealed no reference in to the work presented here. The reader can consult the broad survey by W. A. Gardner [1] on cyclostationarity in different application domains and more recent studies of the indicators of mechanical cyclostationarity using high-order spectra [2-5]. The tools proposed here have been implemented considering the gearbox cyclostationarity as the targeted signal. Most common gearbox cyclostationarity can be explained as the successive vibration shock pattern of gears. When more than one gear stages are present, considering misalignment and bearing contribution, many cyclostationarities contribute to a vibration signal which appears as a jumble of superimposed shock patterns. In the time domain, a first-order cyclostationarity appears as a repetitive pattern. A second-order cyclostationarity exhibits a statistical repetitive time pattern usually phase-locked with a first-order cyclostationarity, e.g. a pump generates a cavitation noise as the propeller blade passes. Although the proposed tools address first-order cyclostationarities, their signal input can be processed (e.g. envelope detector after removing first-order cyclostationarities) in order to also address higher-order cyclostationarities.

Since it is unrealistic to explain a coded algorithm in detail, mathematical expressions are presented only for the main stream of algorithms. The author hopes that the following description allows a person skilled in signal processing to reproduce the proposed tools. The LabView™ source code is available upon request.

The efficiency of a signal-processing tool is a function not only of coded mathematical expressions but also of the coding efficiency and the user interface. Most papers presented these days emphasize the first aspect and neglect the others. In fact, the second aspect, coding efficiency, cannot be illustrated easily in a paper since the details found in a programming code are far too numerous. Only a few points are given here about how to increase the coding efficiency. To address the last aspect, the paper illustrates some graphical results with the corresponding user interface.

After a short explanation about the phase blur which impairs the high-order spectrum, four time-domain cyclostationarity tools are presented followed by the gear mesh graphic interface.

2 High-order spectra and phase blur

High-order spectra are proposed as indicators of nonlinear mechanical behavior [6]. Used in crack detection [7,8] bispectrum and bicoherence work well with simulated data but fail with measured data on real cracked beams [9]. High-order spectra are also proposed as indicators of mechanical, mainly gearbox, cyclostationarity [2-5]. The following development argues that high-order spectra show some drawbacks when the operating conditions are time-varying. This will be done only for the third-order spectrum but it could be reproduced for any other order.

The third-order correlation

$$M_{3\times}(\tau_1,\tau_2)=\mathrm{E}\{x(t)\cdot x(t+\tau_1)\cdot x(t+\tau_2)\}, \tag{1}$$

where $x(t)$ is the continuous time signal and τ_n is expressed in seconds, has the corresponding third-order estimated spectrum

$$\widehat{C}_{3\times}^{\alpha}(\tau_1,\tau_2)\overset{N\to\infty}{=}\frac{1}{N}\sum_{n=0}^{N-1}x_c(n)\cdot x_c(n+\tau_1)\cdot x_c(n+\tau_2)\cdot\exp(-j2\pi\cdot n\alpha),\ 0<\alpha<0.5 \tag{2}$$

with $\{\tau_1,\tau_2\}$ expressed as a number of samples and where

$$x_c(n)=x(n)-M_{1x}(n) \tag{3}$$

is the discrete signal without the synchronous average contribution $M_{1x}(n)=E\{x(n)\}$. Consider the simple analytical case of $x_c(n)$ defined as

$$x_c(n)=\prod_{k=0}^{2}A_k\cdot\exp(j2\pi f_k\cdot n+\theta_k). \tag{4}$$

An analytic function is considered here only to keep the demonstration simple. (A real field case is far more complex. For example, in a real field case, *k*=0,1,2 can correspond to the contribution of a bent shaft rotation, a gear mesh and rotation of a bearing cage respectively.) From the simplified analytic form, the high-order spectrum can be written as

$$\begin{aligned}\widehat{C}_{3\times}^{\alpha}(0,0)&\overset{N\text{ finite}}{\approx}\frac{1}{N}\sum_{n=0}^{N-1}\Big[\left(A_0\cdot\exp(j2\pi f_0\cdot n+\theta_0)\cdot A_1\cdot\exp(j2\pi f_1\cdot n+\theta_1)\cdot A_2\cdot\exp(j2\pi f_2\cdot n+\theta_2)\right)^3\\&\qquad\cdot\exp(-j2\pi\cdot n\alpha)\Big]\\&\overset{N\text{ finite}}{\approx}\frac{1}{N}\sum_{n=0}^{N-1}(A_0A_1A_2)^3\cdot\exp\left(j2\pi\left(3(f_0+f_1+f_2)-\alpha\right)\cdot n+3(\theta_0+\theta_1+\theta_2)\right)\end{aligned} \tag{5}$$

with the maximum

$$\widehat{C}_{3\times}^{\alpha}(0,0)\overset{N\text{ finite}}{=}(A_0A_1A_2)^3\cdot\exp\left(3(\theta_0+\theta_1+\theta_2)\right)\ \text{for}\ \alpha=3\sum_{k=0}^{2}f_k\ . \tag{6}$$

When considering the ideal case of infinite stiffness (shaft, support, joint, gear...) and no mechanical gap, in an *M* high-order spectrum the phase relation $\theta_0+\theta_1+\ldots+\theta_{M-1}$ cannot be modulated by operating conditions like the load, temperature or rotational speed: the cyclo-relation between mechanical events (e.g. tooth shock) remains constant. The non-ideal case shows some compliance and gaps with the result that the operating conditions modulate the phase relation. The averaging $N\to\infty$ done through different operating conditions blurs the phase relation. Inserting the phase blur $B_n(n)$ in the latter equation yields

$$\widehat{C}_{3\times}^{\alpha}(0,0)\overset{N\text{ finite}}{=}(A_0A_1A_2)^3\cdot\exp\left(3\left(\theta_0+B_0(n)+\theta_1+B_1(n)+\theta_2+B_2(n)\right)\right). \tag{7}$$

For example, in a static condition, if the nominal torque is reversed at the input of the reducer gearbox with the output clamped, the input shaft can turn on many degrees. This shaft rotation capacity must be related to the 0-360° cycle corresponding to a single tooth period: a ten-degree rotation of an eleven-tooth gear corresponds to 110° of tooth period. In real dynamic operating conditions, the applied torque includes a random part introducing a random flexural rotation alignment between gear stages: a blur appears in the cyclo-relation between mechanical events. A blur of ±30° destroys most of the cyclostationarity information. In addition, the 3× product in the exponential argument of eqs. (5)-(7) increases the sensitivity of the third-order spectrum: a phase blur of 10° is enough to lose the information.

When an internal torsion mode is excited, the phase blur can dramatically increase. Bearings and mechanical support gaps make their own contribution to the blur but the worst contribution may come from the rotating gaps (tooth gap) when the torque shows an alternating behaviour. The latter gaps are also a

function of the temperature condition. Gap stiffness and damping are a function of the lubricant viscosity, also driven by the temperature condition.

Used for sampling synchronization, a key phasor located at one end of a gear box maximizes the phase blur observed at the other end: a better practice, but not applicable in the field, is to fix the key phasor in the mid-stage of the gear box.

This latter demonstration of phase blur done for a third-order spectrum can be transposed for different cumulants of a cyclostationary process. The obvious way to reduce phase blur is to sum an integer number of cyclostationarity cycles in the same operating condition observed over time. The other approach proposed in this paper to minimize the blur is to resample the signal. However, sampling a signal synchronously with the rotation angle introduces a phase blur of the impulse response. Natural frequencies related to the damped free response are artificially modulated by a synchronous sampling, impairing the phase coherency of the average of the impulse response estimated from multiple shaft rotations. The phase blur of the tail of the impulse response is a problem for large speed variations and increases apparent damping. For small speed variations, the damping increase is not perceptible with synchronous sampling but the phase blur of cross-spectral-components is still a problem without synchronous sampling.

3 Short-time cumulant sweep analyzer: cyclogram

Z.K. Zhu et Al. have proposed the double-time synchronous averaging (DTSA) [10] which shown some similarities with the proposed cyclogram. The short-time cumulant sweep analyzer, the so-called cyclogram, appears to be a simple tool useful for taking a first look at the signal and finding first-order cyclostationarities. The result is accurate when the observation window corresponds to a stationary operating condition. In practice, a long period of cyclostationarity calls for a long observation window with typically, at least 10 to 30 cumulated periods needed to fix the cyclostationarity pattern. In the case of some signals, however, the operating condition does not appear sufficiently stable to obtain an accurate result for a long cyclostationarity period. Moreover, if the signal is not sampled synchronously, the rotation speed fluctuation impairs the results.

The cyclogram of an x_i finite-time series is defined as the graphic illustration of the cumulant

$$C_{N,n} = \frac{1}{M}\sum_{m=0}^{M} x_{n+N\cdot m}\ ,\ n \in [0, N-1] \text{ and } M = \lfloor Ntot / N \rfloor, \tag{8}$$

with the RMS marginal

$$C_N = \sqrt{\frac{1}{N}\sum_{n=0}^{N} C_{N,n}^2}\ , \tag{9}$$

where $\lfloor * \rfloor$ is rounded toward infinity, *Ntot* is the total number of samples and *N,* the cyclostationarity period expressed as number of samples. Illustrated on an intensity x-y graph with the period on the x-axis and time on the y-axis, the cyclogram shows a triangle containing vertical bars. Cyclostationarity corresponds to a strongly contrasting vertical pattern of higher-amplitude bars. Non-stationary cyclostationarity has thicker corresponding bars. Figure 1 gives an example of a cyclogram obtained for a reducer gearbox where at least six cyclo-components are visible. Cyclostationarity could be viewed as a combination of two separate cyclo-stationarities each driving a harmonic-period series of cyclo-components appearing on the RMS marginal graph (Fig. 1, bottom graph). The first coincidence of these components corresponds to the Least Common Multiple (LCM) of the two periods. Usually, this component has the higher amplitude level and corresponds to the desired cyclostationarity. The user looks for high-amplitude components and some relation between observed periods and the equipment datasheet. In fact, when the period of a combined cyclostationarity corresponds to a non-rational multiple number of rotations (e.g. bearing cage rotation or inductive-motor rotor slip angular frequency), the LCM is infinite and the cyclogram does not yield well the information.

Since the step resolution in the cyclogram sweep is limited by the sample period, time signal interpolation is recommended in order to obtain an accurate result (Fig. 2). Note that, with synchronous sampling, the gear cyclostationarity period corresponds to an integer number of time samples but this coincidence does not exist when the cyclostationarity involves a bearing cage period. In the case of non-synchronous sampling, none of the cyclostationarity periods corresponds to an integer number of time samples: interpolation is needed to obtain a close match between an integer number of samples and the cyclostationarity period. Also, the interpolation factors must be increased to take into account the case of short periods (far right side of the cyclogram).

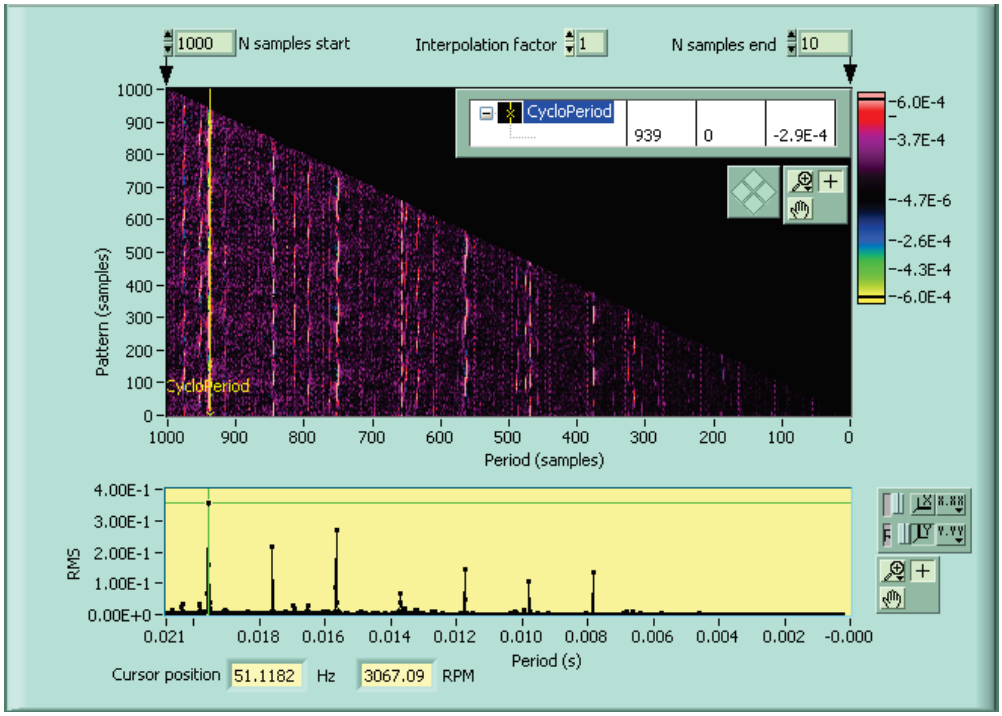

Figure 1: Cyclogram of vibration signal captured on a reducer gearbox (top graph) and the corresponding marginal RMS value (bottom graph). The *n*=939 sample period shows a clear cyclostationarity corresponding to 51.1 Hz. The *n*-period sweep range is fixed from 1000 to 10 samples.

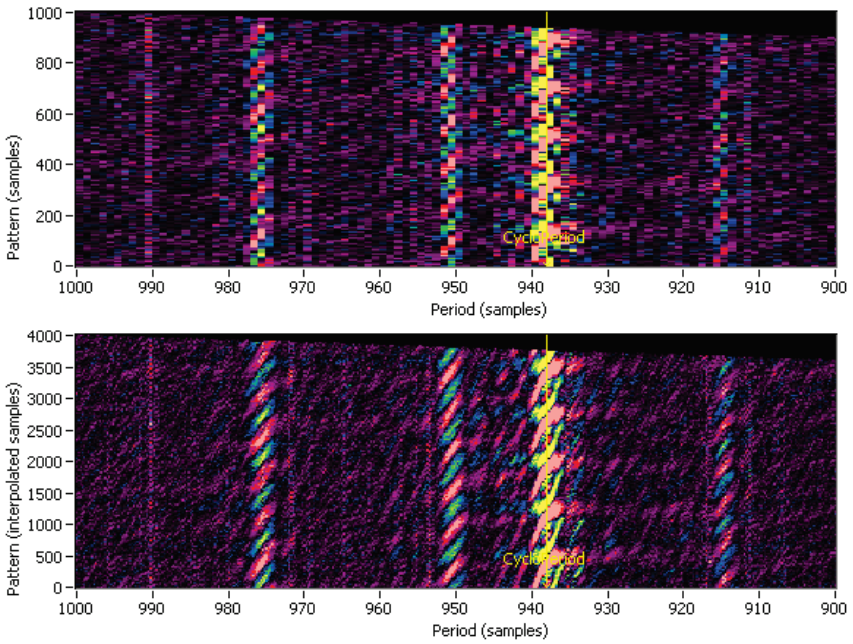

Figure 2: Example of the impact of the interpolation factor on a cyclogram. Zoom of the cyclogram illustrated in Fig. 1 for an interpolation factor of 1 (top) and 4 (bottom). The x-axis uses the same original sample period before interpolation when the y-axis is referenced to an interpolated sample period.

When cyclostationarity is found, it can be removed from the original signal. The RMS ratio of the (signal-cyclostationarity)/signal gives a useful indication of the relative importance of the cyclostationarity and of the accuracy of the cyclostationarity pattern estimation. Figure 3 (top) shows the cyclostationarity pattern corresponding to the cursor position in Fig. 1-2. Figure 3 (bottom) illustrates the result of removing the cyclostationarity pattern, which accounts for about 40% of the vibration power. Figure 4 shows the cyclostationarity corresponding to a better result obtained for a 2438-sample period contributing 45% of the vibration power. As for interface functionalities, when the user moves the cursor on the cyclogram (Fig. 1, top) the cursor of the marginal RMS follows (Fig.1, bottom) and the pattern (Figs. 3-4, top) is updated in real

time. When the removed pattern function is activated, a CPU time delay may occur and the resulting signal is shown (Figs. 3-4, bottom graph and RMS reduction ratio value).

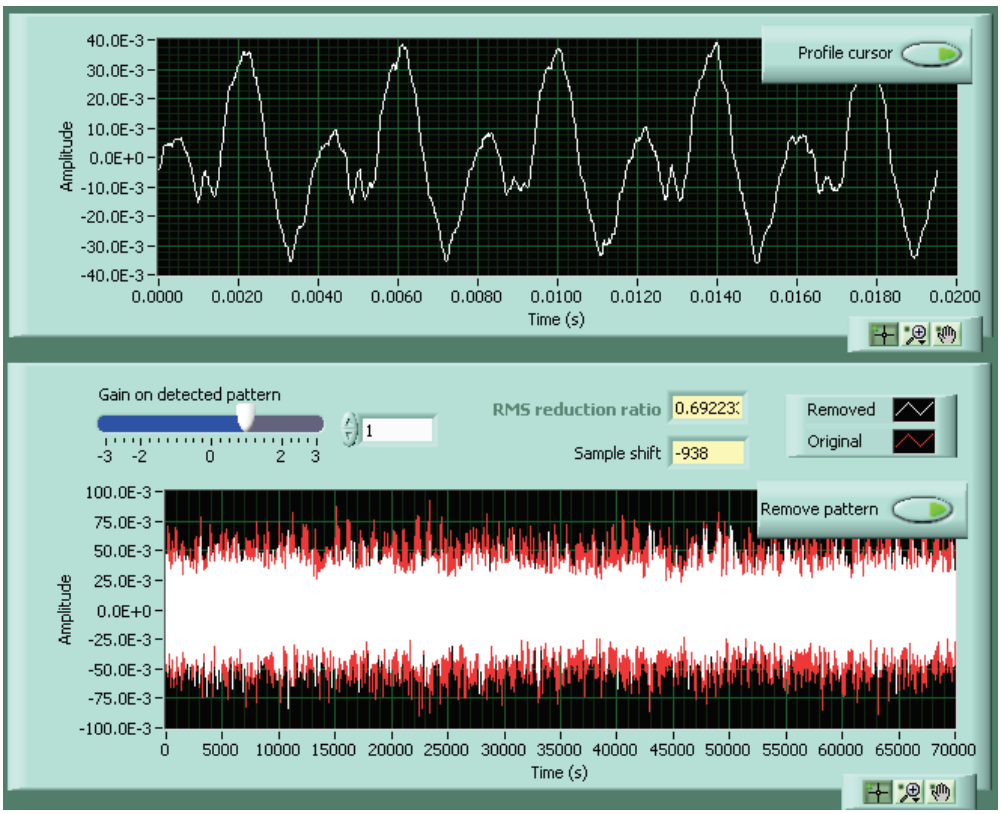

Figure 3: Cyclostationarity pattern (top) corresponding to the cursor position 939 on Fig. 1 and the resulting signal after pattern removal (bottom white curve).

4 Parametric resampled time signal

To overcome unstable operating conditions and/or deal with unsynchronized sampling, parametric resampling can track a cyclostationarity over time. The proposed manual tool addresses short durations using a polynomial expression to model the time transfer function. The cumulant

$$C_{N,n} = \frac{1}{M}\sum_{m=0}^{M} x'_{n+N\cdot m}\ ,\ n \in [0, N-1] \text{ and } M = \lfloor Ntot / N \rfloor, \tag{10}$$

of a cyclostationarity pattern is extracted from the resampled signal x'_n. Using the windowed Whittaker–Shannon interpolation formula,

$$x'_n = \sum_{j=-J/2}^{J/2} x_{n+j+\lfloor d_n+0.5 \rfloor} \cdot w_j \cdot \mathrm{sinc}\left(d_n - \lfloor d_n + 0.5 \rfloor\right) \tag{11}$$

is the resampled signal where w_j represents window coefficients and d_n are time-warping coefficients. Note, no warping occurs when $d_n = n$. A Gaussian-shaped spectral window is used. Note that the half-sample maximum offset between window and sinc function introduces a negligible effect when J>30. Less accurate, spline interpolation can also be used instead of eq. (11) to overcome the computational expenditure. The interpolation, typically 2× to 5×, is done before resampling. It increases the accuracy of all resampling including spline resampling. Note that the interpolation is done just once, after data reading, whereas resampling is done many times in the optimization process. Time-warping coefficients are adjusted to maximize the x'_n RMS marginal (eq. 9). Since there is no closed-form solution, we are compelled to find the maximum numerically using an iterative search where the time-warping coefficients are generated by a second-order polynomial function. The polynomial function generates $N \cdot M$ time-warping coefficients in order to fit the required number of samples to feed eq. 10. Indeed, in the coded algorithm, one left and one right time-sample buffer are allowed for interpolation (J samples) and for considering the maximum parametric excursion range of time-warping sample generation.

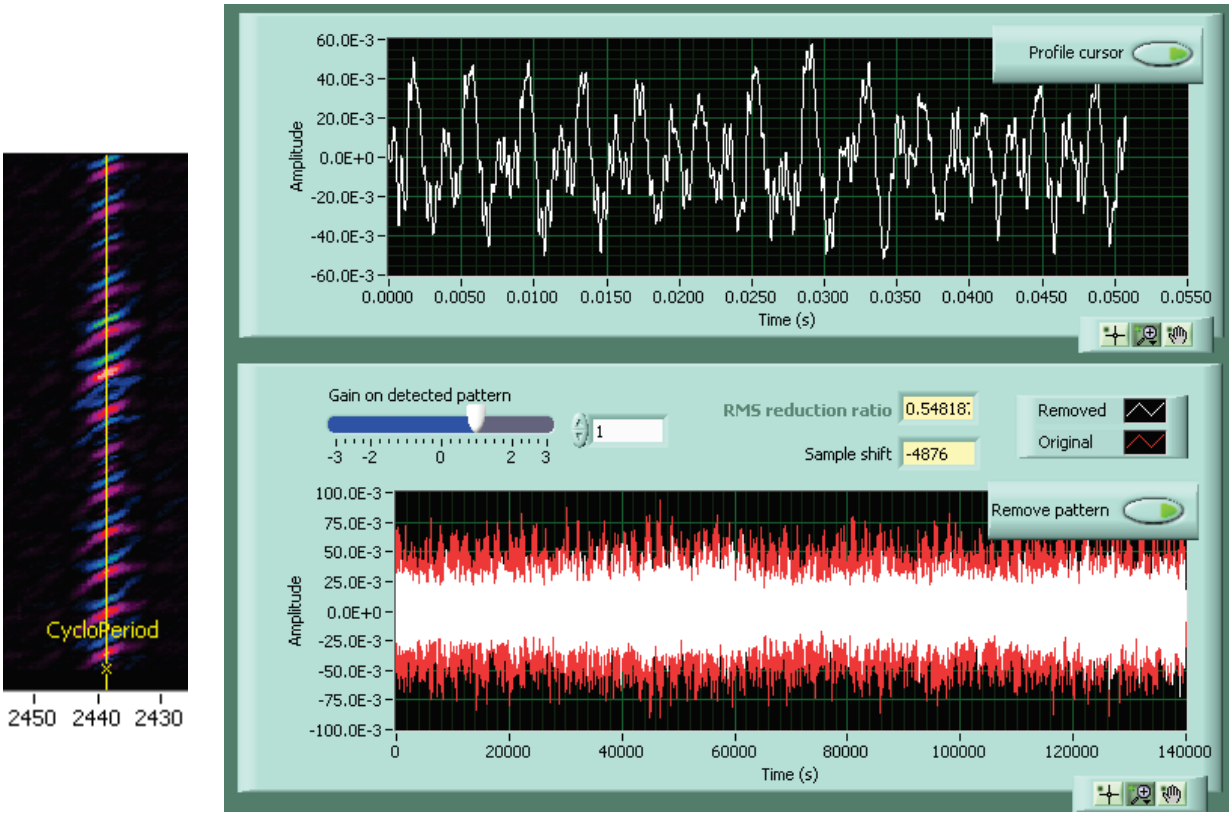

Figure 4: Cyclogram component observed for period 2438 (left) and the corresponding cyclostationarity pattern (top) and the resulting signal after pattern removal (bottom white curve)

Figure 5 illustrates the main part of the user interface. The user selects the interpolating factor (not shown in this figure), the number of iterations, the relative speed range variation, the maximum number *M* of summated cycles and the tracking period *N*. If the number of iterations allowed is sufficient when turning the tracking period button, the graphic stabilization time response appears as a function of the product of the speed variation range with the number of summated cycles. In practice, for a long-period cyclostationarity like the one illustrated in Fig. 5, the time response is about 2 s which seems to be the user-friendly limit. A cyclostationarity component is revealed by an increase in the amplitude and contrast on the graph and, also, in the ratio of the component RMS over the signal RMS. The feature for removing the cyclostationarity from the initial signal is also available with graphic illustration and save option. The time-warping second-order polynomial curve is also shown on another graph (not illustrated in Fig. 5).

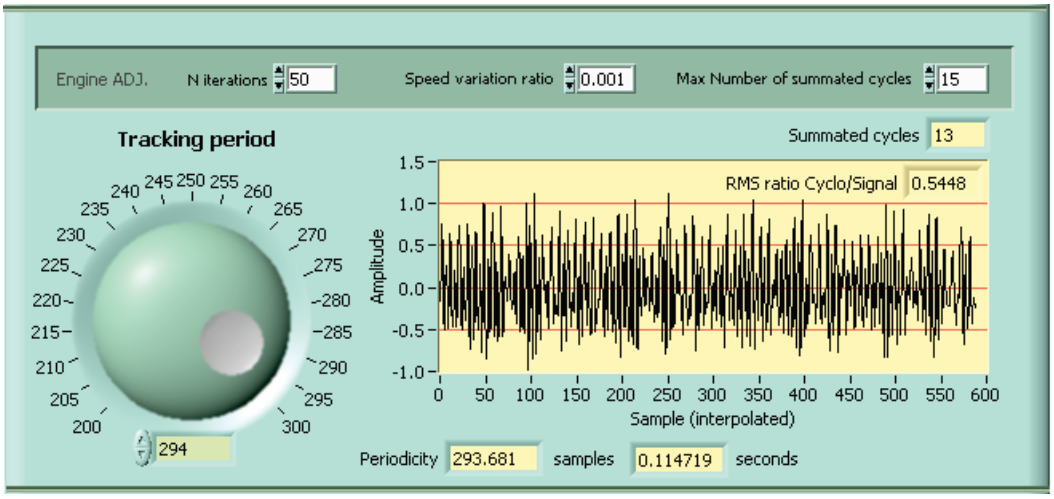

Figure 5: Cyclostationarity component found for period 293.685 and observed over 13 cycles for a total of 3818 samples. Tracking period button and estimated periodicity are expressed as the number of samples when the x-axis on the graph is expressed in interpolated samples (2× interpolation here).

This manual "tuner" appears time-consuming when a large range of periods is to be analyzed. The main drawback is the limited time-warping offered by a single second-order polynomial function. The next proposed tool addresses these two drawbacks.

5 Cyclostationarity matching pursuit with adaptive resampled signal

In order to overcome unstable operating conditions over a long period of time, parametric time-warping is modeled by successive polynomial curves. The tool process comprises four stages. In the first stage, a cyclostationarity sweep is done for a predetermined range (*CSR*) fixed by the user (e.g. sweep period from 100 to 300 samples) with a predetermined sweep step length (e.g. every 2 samples). The user also fixes the interpolating factor, the number of iterations (*NI*), the relative speed range variation (*SR*) and the maximum number *M* of summated cycles. In the second stage, the RMS ratio of the result of the sweep is shown on a graph (Fig. 6) and the user selects a component, usually the one with the greatest amplitude. For a given step in the sweep, the relative speed range variation allows a matching range in ±samples from this period. When the sweeping step is set too fine, like that in Fig. 6, the same result can be found for many successive sweeping steps. In the third stage of the process, the pursuit algorithm is initialized with the user-selected component and launched with a new set of tracking parameters (*CSR*, *NI*, *SR* and *M*) also fixed by the user. The pursuit algorithm is a loop where each match result is used as a feeder for the next match. A match result includes the last cyclic pattern, the last period length expressed in number of samples (not resampled) and the cumulant of the squared amplitude of the cyclic pattern. The last cumulant is used to generate the coherency. The coherency

$$\gamma^2_{N,n,M} = \left(\sum_{m=1}^{M} C_{N,n,m} \right)^2 \Big/ M \cdot \sum_{m=1}^{M} \left(C_{N,n,m} \right)^2 , \tag{12}$$

with *M* the current number of summated cycles, appears an accurate estimator of the pattern repeatability through time: sometimes only a part of the pattern is disturbed by the changing operating conditions and this estimator allows to pinpoint the disturbed part. During the matching pursuit process, the coherency result is superimposed on a graph with the last pattern like that in Fig. 7. The coherency has its maxima between zero crossings and drops at zero crossing. Any unstable part of the pattern shows a dip in the maxima in the corresponding part. For example, a small dip is observed around sample 440 in Fig. 7. The coherency maxima shown in the same figure are mostly higher than 0.85, an excellent result which is explained by the stability of the component like that in Fig. 8 where the component period stays within the range of the fraction of a sample.

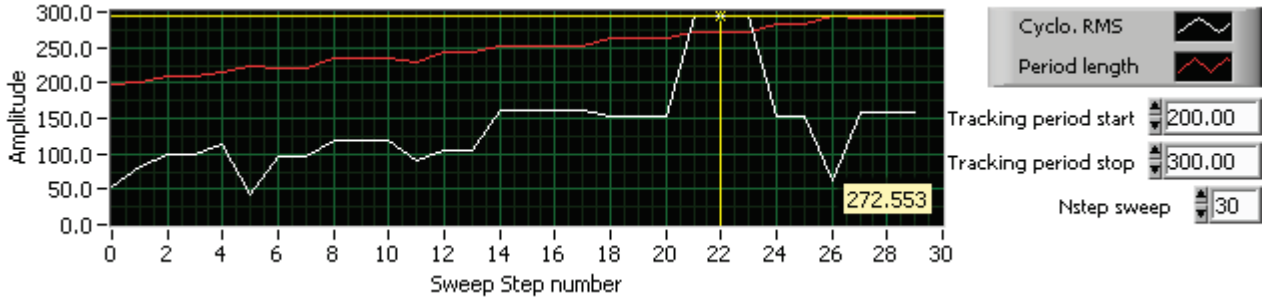

Figure 6: Cyclostationarity sweep result obtained for a sweep starting at 200 samples and ending at 300 samples. The RMS scale is adjusted to fit the maximum length of the period. In this example, the redundant result obtained on the summit is due to the small sweep step selected.

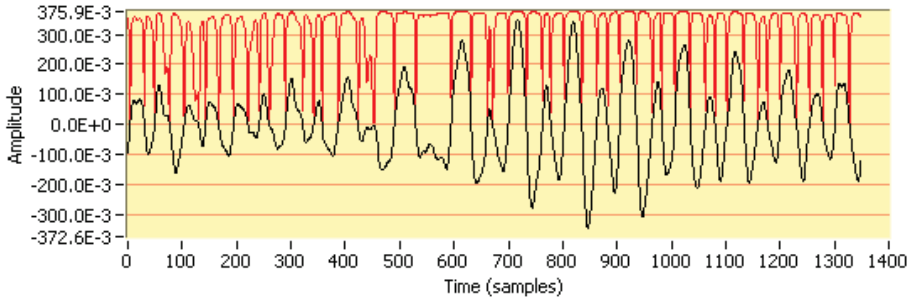

Figure 7: Last estimated cyclostationarity pattern (black) and overall coherency (red) obtained after more than 1000 estimated periods. The coherency is plotted in the half upper part of the graph with a 0 to 1 full-range scaling.

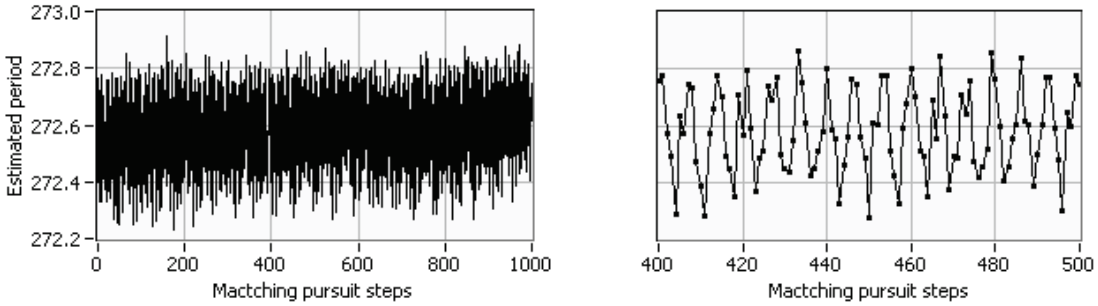

Figure 8: Time evolution of the estimated component period for more 1.5 E 6 time samples (5.5 min) and zoom of a 100-step section.

As with the last two tools, the resulting cyclostationarity can be subtracted from the original signal. Figure 9 illustrates an example of the original signal related to figures 6-7 and the corresponding residu after the first order cyclostationarity removal. Before doing this, the signal is resampled step by step considering the estimated period. The actual tool considers only the final averaged cyclostationarity in subtraction but, as a future feature, the "in-progress moving average cyclostationarity pattern" can be used in order to yield a better component removal. A long period modulation generated by a cyclic load or due to some other mechanical phenomenon (e.g. coincidence with a bearing cage) exhibits a cyclic oscillation in the tracked pattern. This cyclic oscillation is visible in the pattern and/or the estimated period graph when its period appears longer than two matching steps like the oscillation visible in the right graph of Fig. 8.

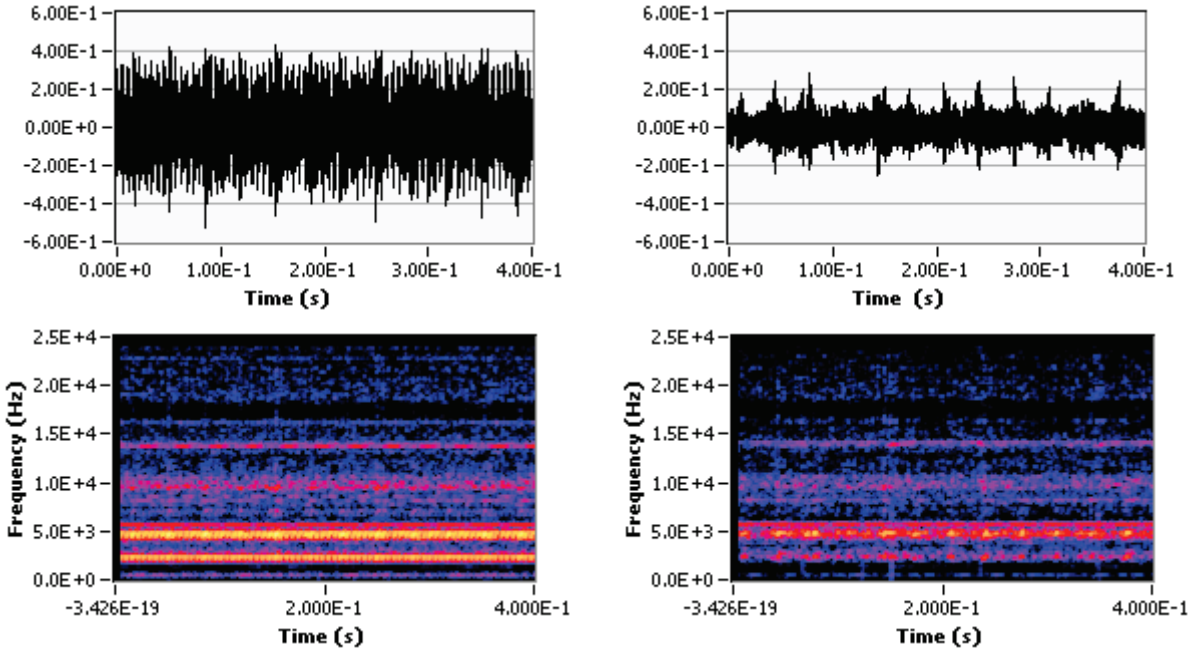

Figure 9: (Left) Original signal and the corresponding spectrogram. (Right) Residu signal and the corresponding spectrogram after the removal of the first order cyclostationarity.

6 Fragmented-signal synchronous summation

In a gearbox, if we exclude the rotation bearing cages, the first-order cyclostationarity is presented as a multiple of its teeth. For a cyclostationarity having *I* tooth shocks, the algorithm counts the passage of each tooth, determines the total and produces the average tooth pattern for each tooth. The cyclostationarity pattern is composed of the concatenation of the average patterns of *I* tooth shocks.

Figure 10 presents the flowchart of the "fragmented-signal synchronous summation" algorithm developed for measurements where impacts are clear. Conditioning the time signal offers several choices as a band-pass or high-pass filter, an envelope, a derivative or an integration calculation. Conditioning of the time signal may be different for the signal feeding the threshold comparison. Interpolation is essential for an accurate estimation of the impact pattern: the main half-impact lobe should include several samples. This algorithm works only for cases where the tooth impact allows the use of a simple threshold crossing to detect most of the passages of the teeth. A period of passivity disables the tooth-pass detector for a delay longer than the tooth shock response and shorter than the shock-to-shock period. Not shown in Fig. 10, the algorithm forces a tooth-pass detection when a maximum time is reached in order to avoid missing a tooth when the tooth response exhibits a low amplitude, below the threshold level. Once the impact of a tooth is detected, the algorithm increments the tooth counter and the tooth pattern is added to the corresponding tooth number summation pattern. Cyclostationarity is complete once the tooth count reaches *I* teeth, whereupon the tooth counter is reset. The algorithm stops when there are no more samples to be treated. Also not shown in Fig. 3.1 is an anticipatory period (pre-trigger value) which allows the summation of the tooth pattern to begin before the threshold is exceeded.

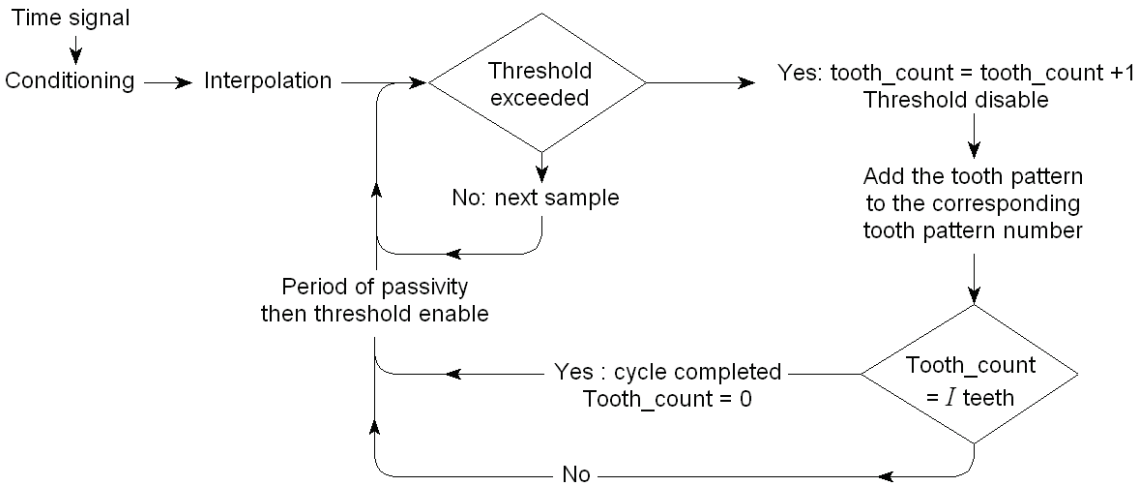

Figure 10: Flowchart of the fragmented-signal synchronous summation algorithm required to obtain the average of a cyclostationarity impact pattern.

One feature is to add a correlation or maximum detector after the threshold logic box illustrated in Fig. 10. This increases the location accuracy of the beginning of the pattern and can be implemented in fragmented signal synchronization or in the gear mesh graph (following section).

In its current state the algorithm calls for patience and experience because of the many parameters to be adjusted before a decent result is obtained. Success comes in part from the selection of the trigger threshold level. We have added a graphical tool that displays distances (in number of samples) between two successive detected shocks (Fig. 11 top left). This is to adjust the threshold, the time passiveness and the maximum distance so that no significant increase is observed in the distance between consecutive shocks. When a shock is missing, the corresponding distance between the shock before and that after the missing shock is double in length.

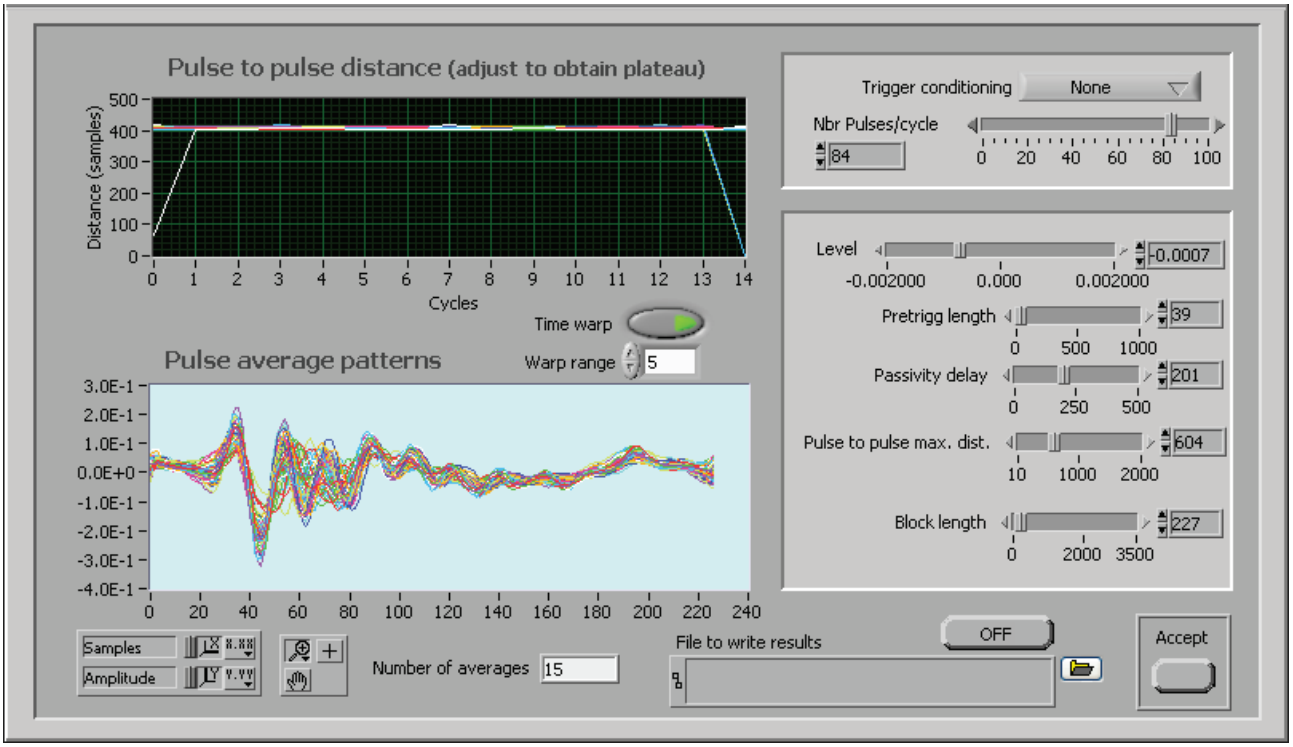

Figure 11: Fragmented-signal synchronous summation algorithm, front end. The right parameters are adjusted in order to obtain a constant distance on the upper graph.
Tooth average patterns are superimposed on the bottom graph.

7 Gear mesh graph

Some interesting results are generated by the graphical presentation of the gear mesh pattern. The 3D cascade of the gear mesh cyclostationarity is built by stacking the successive shock responses, as illustrated in Fig. 12. Figure 13 shows the gear mesh for an observed cyclostationarity of 84 impacts. Here, we assume that the pulse or impact corresponds to a tooth shock. This 3D graph depicts the instantaneous amplitude as a function of time (horizontal) and the shock number (vertical). In fact, if the block length is enough to include more than one tooth response, we can see the same pattern reproduced in time with one tooth less at each response like in the right pattern in Figs. 13 and 15. Note that the Fig. 13 pattern can be divided into four vertical concatenate patterns suggesting diagnostic possibilities. A gear mesh graph can show eccentricity, nonuniform gear loading (radial or tangential) or a damaged tooth. The presence of a cyclostationarity associated with a set of processing parameters is detected by the sharp 3D pattern contrast corresponding to a coherently summated shock pattern. This last criterion of visual contrast appears subjective; we propose calculating the coherence as a discrimination tool to detect cyclostationarity.

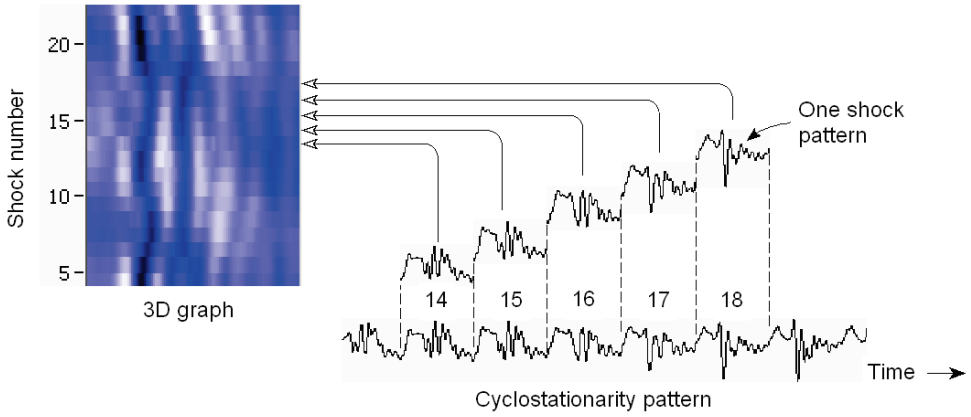

Figure 12: 3D graph of a gear mesh obtained by stacking the temporal shock tooth responses.

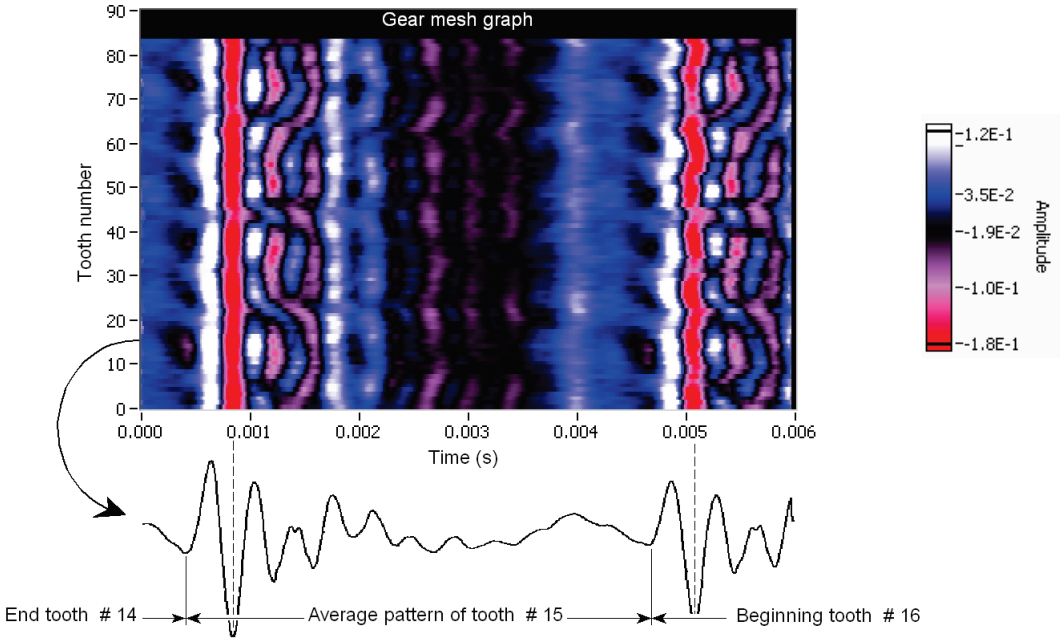

Figure 13: Pattern of average impact over 29 cycles of a cyclostationarity with a length of 84 impacts. The positive peaks are white, the negative red.

The cyclostationarity average pattern is segmented into I impacts where I is fixed by the user. The I impact segments, each corresponding to a different tooth-to-tooth shock, can be time-aligned with an over-threshold, with a rising edge or with a correlation on the beginning part of the impact. With the fragmented-signal synchronous summation, the impact alignment is done individually for each impact corresponding to a given tooth. For the latter case, if n_{im} is the vector containing the starting position for impact number "i" and cycle "m", the average pattern of the impact of "i" is written as

$$\mathbf{P}_i(n) = \frac{1}{M}\sum_{m=1}^{M} x_{n+n_{im}} \ , \quad n \in [0, B-1] \tag{12}$$

where n is the time in number of samples and B is the buffer length covering at least one tooth shock length, i.e. $B \geq N / I$. When the pattern is generated by a resampled time signal, the tooth-to-tooth distance is constant: the cyclostationarity pattern $C_{N,n}$ is divided into I equal-length segments. For the fragmented synchronous summation, the i^{th} impact has the following coherency:

$$\gamma_i = \frac{\left|\mathbf{P}_i\right|}{\left(\sum_{n=0}^{B-1}\sqrt{\sum_{m=1}^{M} x_{n+n_{im}}^2}\right)} = \frac{\sqrt{\sum_{n=0}^{B-1}\left(\frac{1}{M}\sum_{m=1}^{M} x_{n+n_{im}}\right)^2}}{\left(\sum_{n=0}^{B-1}\sqrt{\sum_{m=1}^{M} x_{n+n_{im}}^2}\right)} \ . \tag{13}$$

Figure 14 shows the distribution of the tooth coherency corresponding to Fig.13 while the following figure depicts the gear mesh graphic interface used to process cyclostationarity obtained with a cyclogram with or without a resampled time signal. The user manually adjusts the number of teeth per cycle, the buffer time length and the tooth offset position when the graph is continuously refreshed. The graph in Fig. 15 corresponds to the result in Fig. 5 for a long buffer: only the first vertical pattern must be considered here as the actual gear mesh pattern; the other patterns are just replicas with a tooth shift. The uniform contrast of replica patterns demonstrates that for small speed variations the phase blur of the impulse response is not perceptible with synchronous resampling. Note that some works [11] have proven that a high-coherency well contrasted component may not correspond to a real cyclostationarity. The user has to consider the possibility of an artefact component, none mechanically related.

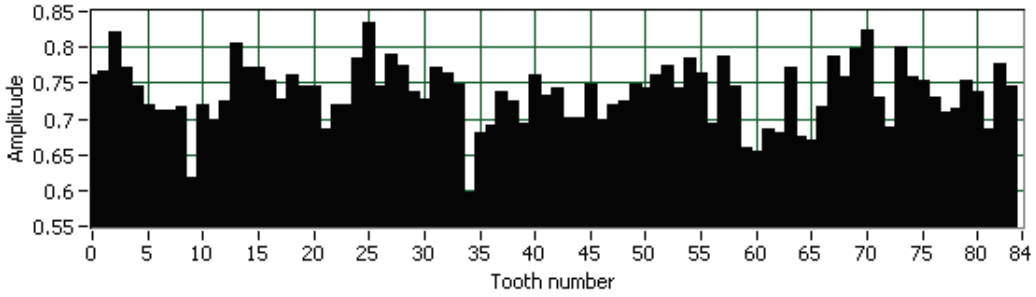

Figure 14: Coherency tooth pattern of the 84-impact cyclostationarity seen in Fig. 11.

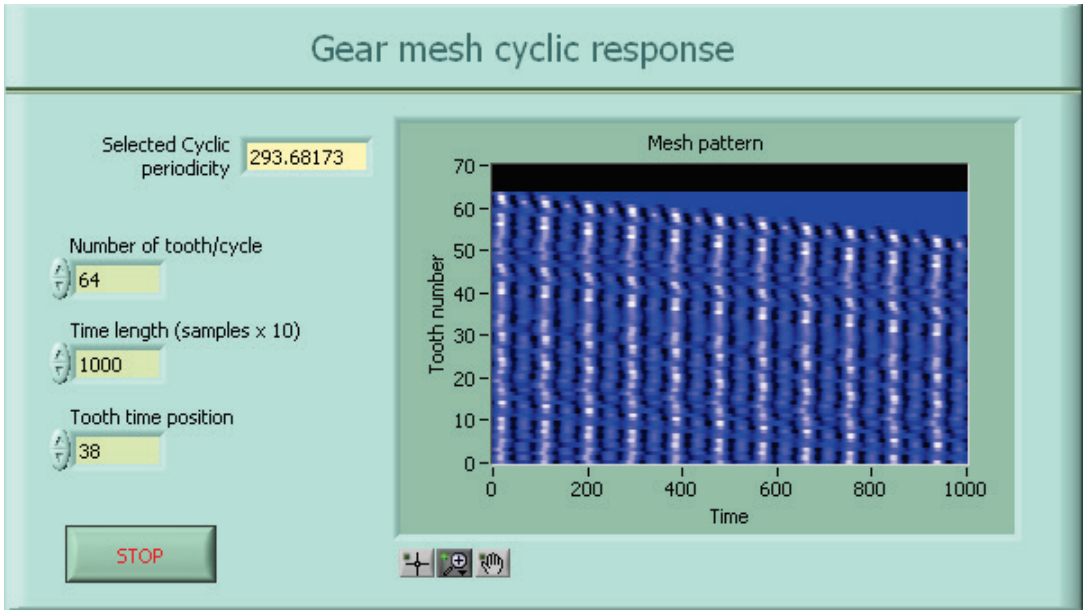

Figure 15: Gear mesh graph of the cyclostationarity component found for the period 293.681 in Fig. 5. Note that the pattern is 10× interpolated.

8 Conclusion

Time domain methods show interesting results and appear as an alternative to the spectrum approach in cyclostationarity detection and characterization. The time domain coherency indicators proposed are useful for detecting a cyclostationarity and analyzing the time pattern repeatability. The 3D gear mesh graph proposed to illustrate a cyclostationarity gives an accurate picture of the uniformity of the tooth shock pattern and can be relevant for diagnostic purposes. The algorithms and user interface ideas presented here are elements of the first deployment of the time domain cyclostationarity approach: many improvements are to be found. In the short term, the spectrum approach and the time domain approach must be compared by means of case studies and involve the participation of skilled researchers in the domain. Signal adaptive resampling used in the time domain approach can be also used to reduce the phase blur of spectral components in the spectrum approach.

References

[1] W. A. Gardner, *Cyclostationarity in communication and signal processing*, IEEE Press, New York (1994).

[2] G .Lejeune, J. Lacoume, P. Marchand, M. Durnerin, N. Martin, J. Liénard, A. Silvent, C. Mailhes, P. Prieur, G. Goullet, *Cyclostationnarités d'ordre 1 et 2 : application à des signaux vibratoires d'engrenages*, GRETSI No. 16, Grenoble, France (1997), pp. 323-326.

[3] A, Raad, J. Antoni, M. Sidahmed, *Indicators of cyclostationarity: proposal, statistical evaluation and application to diagnostics*, ICASSP 2003, Hong Kong, China (2003), Vol. 6, pp. 757-60.

[4] J. Antoni, F. Bonnardot, A. Raada, M. El Badaoui, *Cyclostationary modelling of rotating machine vibration signals*, Mechanical Systems and Signal Processing 18 (2004), pp. 1285–1314.

[5] A. Raad, J. Antoni, M. Sidahmed, *Indicators of cyclostationarity: Theory and application to gear fault monitoring*, Mechanical Systems and Signal Processing (2008), Vol. 22, No. 3, pp. 574–587.

[6] B. Collis, P. R. White, J. K. Hammond, *Higher Order Spectra: the Bispectrum and Trispectrum*, Mechanical Systems and Signal Processing (1998), Vol. 12, No. 3, pp. 375-394.

[7] D. Choi, J.-H. Chang, R. O. Stearman, E. J. Powers, *Bispectral identification of nonlinear mode interaction*, Proceedings of the 2nd International Modal Analysis Conference, Orlando (1984), pp. 602-609.

[8] A. Rivola, P. R. White, *Bispectral Analysis of the Bilinear Oscillator with Application to the Detection of Fatigue Cracks*, Journal of Sound and Vibration (1998), Vol. 216, No. 5, pp. 889-910.

[9] F.Léonard, J. Lanteigne, S. Lalonde, Y.Turcotte, *Free-vibration behaviour of a cracked cantilever beam and crack detection*, Mechanical System and Signal Processing, (2001), Vol. 15, No.3, pp. 259-548.

[10] Z.K. Zhu, Z.H. Feng, F.R. Kong, *Cyclostationarity analysis for gearbox condition monitoring: Approaches and effectiveness,* Mechanical Systems and Signal Processing (2005), Vol. 19, No. 3, pp. 467–482.

[11] F.Léonard, R. Archambault, *Le diagramme du profil d'impact de dents dans le diagnostic d'un réducteur*, 2010 CMVA-ACVM annual seminar, Oct. 27-29, Québec (2010).